Deutsches Elektronen-Synchrotron DESY

H1prelim-25-031, DIS 2025
March 25, 2025

Towards Unfolding All Particles in High Q^2 DIS Events

H1 Collaboration

Abstract

The differential cross section with respect to all final state particle momenta and electric charge in high Q^2 events is measured in deep-inelastic positron-proton scattering using data collected with the H1 detector of HERA. The unbinned and full phase-space unfolding is implemented using the OmniFold machine learning algorithm, with the point-edge transformer neural network architecture. To illustrate the utility of this measurement, we present a number of projections from the full phase space, including observables previously measured by H1 and new observables that are challenging using conventional methods. For example, we show a simultaneous measurement of jets in the laboratory and Breit frames. The data are corrected for detector acceptance, efficiency, and resolution effects and uncertainties are estimated at the per-particle level and we are working towards releasing the result in an unbinned format.

1 Introduction

High Q^2 deep inelastic scattering (DIS) data have diverse utility in particle and nuclear physics. These data have been used to study event and jet shapes, probe nuclear structure, and much more [1]. Each result is presented as a separate measurement, often in the form of a binned, differential cross-section.

Machine learning has enabled a complementary paradigm whereby the full phase space is simultaneously measured [2]. By extracting the differential cross section with respect to all final state particle properties, observables can be extracted after the measurement instead of before. An essential aspect of these measurements is that they are unbinned. A number of unbinned measurements in hadronic final states have been presented recently by H1 [3–6], LHCb [7], STAR [8,9], ATLAS [10,11], and CMS [12].

This paper significantly extends previous measurements in hadronic final states by simultaneously measuring the spectrum of all final-state particles. This requires machine learning models capable of processing the set of particle momenta and electric charges, which in machine learning is called a variable-cardinality point cloud. The unfolding thus proceeds with the OmniFold method [13, 14] based on the Point-Edge Transformer neural network architecture [15, 16]. The resulting phase space is vast and we are working toward publishing the data in an unbinned format for widespread use. In the mean time, a representative set of observables have been chosen to illustrate the potential of the differential cross section. This set includes observables previously measured, such a lepton-jet azimuthal correlations in the lab frame [3] and jet substructure [5] as well as observables that are challenging to measure using conventional methods, like jet properties measured in different reference frames.

This note is organized as follows. Section 2 introduces the H1 detector and the analysis observables. Then, Sec. 3 describes the Monte Carlo simulated datasets used for the analysis. Corrections for detector effects (unfolding) using the OMNIFOLD algorithm are detailed in Sec. 4. Uncertainty estimation is detailed in Sec. 5. Theoretical predictions using Quantum Chromodynamics (QCD) and experimental results are presented in Sec. 6 and the note ends with conclusions and outlook in Sec. 7.

2 Experimental method

A full description of the H1 detector can be found elsewhere [17–21] while the detector components that are most relevant for this measurement are described below. The main sub-detectors used in this analysis are the inner tracking detectors and the Liquid Argon (LAr) calorimeter, which are both immersed in a magnetic field of 1.16 T provided by a superconducting solenoid. The central tracking system, which covers $15^\circ < \theta < 165^\circ$ and the full azimuthal angle, consists of drift and proportional chambers that are complemented with a silicon vertex detector in the range $30^\circ < \theta < 150^\circ$ [22]. It yields a transverse momentum resolution for charged particles of $\sigma_{p_T}/p_T = 0.2\%\ p_T/\text{GeV} \oplus 1.5\%$. The LAr calorimeter, which covers $4^\circ < \theta < 154^\circ$ and full azimuthal angle, consists of an electromagnetic section made of lead absorbers and a hadronic section with steel absorbers; both are highly segmented in the transverse and longitudinal directions. Its energy resolution is $\sigma_E/E = 11\%/\sqrt{E/\text{GeV}} \oplus 1\%$ for leptons [23] and $\sigma_E/E \approx 50\%/\sqrt{E/\text{GeV}} \oplus 3\%$ for charged pions [24]. In the backward region ($153^\circ < \theta < 177.5^\circ$), energies are measured with a lead-scintillating fiber calorimeter [21]. Results are reported using the data recorded by the H1 detector in the years 2006 and 2007 when positrons and protons were collided at energies of 27.6 GeV and 920 GeV, respectively. The total integrated luminosity of this data sample corresponds to 228 pb^{-1} [25].

DIS reactions are governed by the momentum transferred between the lepton and proton squared, Q^2, and the inelasticity y, or equivalently, the longitudinal momentum fraction $x = Q^2/(s \cdot y)$, where s is the center-of-mass energy of the collision. The Σ method [26] is used to reconstruct Q^2 and y as:

$$Q^2 = \frac{E_{e'}^2 \sin^2 \theta_{e'}}{1-y} \tag{1}$$

$$y = \frac{\sum_{i\in\text{had}}(E_i - p_{i,z})}{\sum_{i\in\text{had}}(E_i - p_{i,z}) + E_{e'}(1-\cos\theta_{e'})}, \tag{2}$$

where $\theta_{e'}$ is the polar angle of the scattered lepton and $\sum(E_i - p_{i,z})$ is the total difference between the energy and longitudinal momentum of the entire hadronic final state. Compared to other methods, the Σ reconstruction method reduces sensitivity to collinear initial state QED radiation, $e \to e\gamma$, since the beam energies are not included in the calculation.

Events are triggered by requiring a high energy cluster in the electromagnetic part of the LAr calorimeter. The scattered lepton is identified as the highest transverse momentum LAr cluster matched to a track passing an isolation criteria [27]. Events containing scattered leptons with energy $E_{e'} > 11$ GeV are kept for further analysis, resulting in a trigger efficiency higher than 99.5% [28, 29]. Backgrounds from additional processes such as cosmic rays, beam-gas interactions, photoproduction, charged-current DIS and Quantum Electrodynamics (QED) Compton processes are rejected after a dedicated selection [29, 30], resulting in negligible background contamination. In particular, events with $Q^2 > 150$ GeV^2, $0.08 < y < 0.7$, $p_{\text{T}}^{\text{miss}} < 10$ GeV, and $45 < E - p_z < 65$ GeV and particles with $p_{\text{T}}^{\text{part}} > 0.1$ GeV and $-1.5 < \eta^{\text{part.}} < 2.75$ are selected.

The full phase space is measured, but to highlight the utility of these data, we select a set of jet and event-level observables described below.

The FastJet 3.4.2 package [31, 32] is used to cluster jets. We first cluster jets in the laboratory frame with the inclusive k_{T} algorithm [33, 34] and distance parameter $R = 1$. The inputs for the jet clustering are hadronic final state (HFS) objects with $-1.5 < \eta < 2.75$. These objects are built from calorimeter-cell clusters and reconstructed tracks, after removing those associated with the scattered lepton, using an energy flow algorithm [35–37]. Jets with transverse momentum $p_{\text{T}}^{\text{jet}} > 10$ GeV are selected for further analysis.

The Breit frame, illustrated in Figure 1, is also used in this analysis, simultaneously with the laboratory frame measurements. The Breit frame is defined with the relation $2x_B\vec{P} + \vec{q} = 0$, where $\vec{P}$ is the momentum of the incoming proton and $\vec{q}$ is the momentum of the exchanged virtual photon. In this frame, the struck quark before collision travels along the $+z$ direction with momentum $p_z = \frac{q}{2}$ and then back-scatters with momentum $p_z = -\frac{q}{2}$. The x-y plane is chosen such that the scattered lepton has an azimuthal angle $\phi^{\text{b}}_{e'} = 0$. The boosted HFS four-vectors p^{b} are obtained following the methodology from [38]:

$$p^{\text{b}} = M_{(\phi^{\text{b}}_{e'}=0)} \cdot p^{\text{Lab}}, \tag{3}$$

where p^{Lab} are the four-vectors of the HFS four-vectors in the lab frame and $M_{(\phi^{\text{b}}_{e'}=0)}$ defines the boost when it is chosen that the scattered lepton travels along the x-axis. This matrix is given by:

$$M_{(\phi^{\text{b}}_{e'}=0)} = -\begin{pmatrix} \frac{q_x}{q_T} & \frac{q_y}{q_T} & \frac{q_T}{\Sigma} & -\frac{q_T}{\Sigma} \\ \frac{q_y}{q_T} & \frac{q_x}{q_T} & 0 & 0 \\ \frac{q_x}{Q} & \frac{q_y}{Q} & \frac{q_z}{Q} & -\frac{q_E}{Q} \\ \frac{b_x}{Q} & \frac{b_y}{q_T} & \frac{b_z}{Q} & -\frac{b_E}{Q} \end{pmatrix}, \tag{4}$$

where the boost vector b is

$$b = q - \frac{q\cdot q}{q\cdot\hat{z}}\hat{z}. \tag{5}$$

$\hat{z}$ is $(1;0,0,1)$, $Q^2 = -q\cdot q$, and q is the photon four-momentum. The quantity q is reconstructed as $q = k - k'$, where k' is the scattered lepton momentum and k is the effective lepton beam momentum $k = (\frac{\Sigma_{\text{tot}}}{2};0,0,\frac{\Sigma_{\text{tot}}}{2})$, where Σ_{tot} is the denominator of y in Equation 2. Lastly, $\Sigma = q \cdot \hat{z} = q_E - q_z$.

Jets are clustered in the Breit frame using two different jet clustering algorithms — k_{T} and Centauro [39]. The Centauro jet algorithm is a longitudinally invariant method designed for DIS studies. It employs an

asymmetric distance metric that, in DIS events with configurations close to the Born level (i.e., $\gamma^* q \to q'$) in the Breit frame, successfully clusters the struck-quark jet (see Figure 1, at rapidity $y = -\infty$) while excluding beam remnants (at rapidity $y = +\infty$). Note that such low-p_{T} jets cannot be clustered with the k_{T} (or anti-k_{T}) algorithm (see Ref. [39] for a detailed discussion).

Both clustering algorithms use the distance parameter $R = 1$. The k_{T} jets with transverse momentum $p_{\mathrm{T}}^{\mathrm{jet}} > 5$ GeV are selected for further analysis with the k_{T} algorithm. There is no minimum $p_{\mathrm{T}}^{\mathrm{jet}}$ requirement for the jets clustered with Centauro. Instead, jets with $z^{\mathrm{jet}} > 0.2$, as defined below, are used in this analysis.

The jet observables explored in this analysis are the azimuthal angular distance between the lepton and the jet ($\Delta\phi^{\mathrm{jet}}$) in the laboratory frame using the k_{T} algorithm, similar to Ref. [3]; the jet angularity observable known as jet girth $\ln(\lambda_1^1)$ in the laboratory frame, using the k_{T}, similar to Ref. [5]; the jet transverse momentum $p_{\mathrm{T}}^{\mathrm{jet}}$ using the k_{T} algorithm in the laboratory frame and the Breit frame and using Centauro in the Breit frame; and the fraction of the struck-quark momentum carried by the jet z^{jet} using the k_{T} algorithm in the laboratory frame and the Breit frame and using Centauro in the Breit frame. This is illustrated in Table 1 below:

	Lab k_{T}	Breit k_{T}	Centauro
$\Delta\phi^{\mathrm{jet}}$	Y	N	N
$\ln(\lambda_1^1)$	Y	N	N
$p_{\mathrm{T}}^{\mathrm{jet}}$	Y	Y	Y
z^{jet}	Y	Y	Y

Table 1: Jet observables used in this analysis. Y (N) indicates that observable is (not) calculated for the frame and clustering algorithm in a given column. In addition to these, Δz^{jet} and the Energy-Energy Correlator are measured.

The distributions of the angular distance between the lepton and the jet, jet girth[1], and jet transverse momentum are used to highlight the ability to recover previous results using the unfolded information. Although the particle selection used to select the HFS candidates is changed in comparison to previous measurements, we observe that the results are nevertheless compatible.

In the laboratory frame, z^{jet} is defined as $\frac{P\cdot p^{\mathrm{jet}}}{P\cdot q}$, where P is the proton momentum in the laboratory frame (920 GeV; 0, 0, 920 GeV) and q is the virtual photon momentum. In the Breit frame, z^{jet} is given by $\frac{n\cdot p_{\mathrm{jet}}}{Q}$, where $n = (1;0,0,1)$. This quantity can be compared between frames and jet clustering algorithms by defining:

$$\Delta z^{\mathrm{jet}} = z^{\text{leading jet}}_{\text{lab, } k_{\mathrm{T}}} - z^{\text{leading jet}}_{\text{Breit, Centauro}}, \tag{6}$$

where $z^{\text{leading jet}}_{\text{lab, } k_{\mathrm{T}}}$ and $z^{\text{leading jet}}_{\text{Breit, Centauro}}$ are the z^{jet} of the leading jet from the event clustered using k_{T} in the laboratory frame and Centauro in the Breit frame, respectively. The leading jet is defined as the jet with the highest z^{jet} value. If there are no jets in the laboratory frame for a given event due to the p_T^{jet} cut, that event is skipped when calculating Δz^{jet}.

In addition, we leverage the unique advantage of the methodology to measure Energy-Energy Correlator ($\mathrm{EEC_{DIS}}$), which probes *multi-particle correlations* and is *only* well-defined in the Breit frame [40]. Therefore, $\mathrm{EEC_{DIS}}$ poses a number of fundamental challenges for histogram-based unfolding methods, which are not relevant in this analysis.

First formulated in formal theory [41], the EEC has been found to have widespread utility. (See Ref. [42–48] for review and a list of applications.) Most recently, the EEC has been measured in the cleanest

[1]The jet girth is defined as $\ln(\lambda_1^1)$, where $\lambda_\beta^\kappa = \sum_{i\in\mathrm{jet}} z_i^\kappa \left(\frac{R_i}{R_0}\right)^\beta$, z_i is the ratio $p_{T,i}/p_{\mathrm{T}}^{\mathrm{jet}}$ for a particle with transverse momentum $p_{T,i}$ clustered inside a jet with radius R_0 and momentum $p_{\mathrm{T}}^{\mathrm{jet}}$. The parameter R_i describes the distance between the particle and the jet axis in the transverse plane.

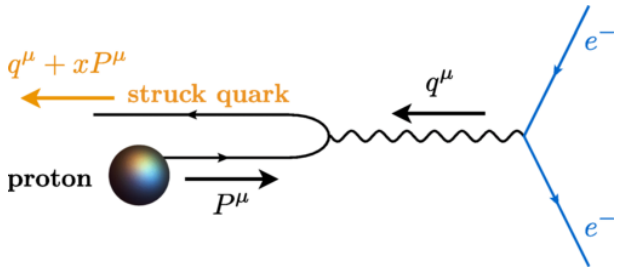

Fig. 1: DIS Born kinematics in the Breit frame. Graphic from Ref. [39].

possible case of e^+e^- collision using the ALEPH data [49]. It then becomes of interest to measure it over the full range of angles in the relatively clean initial state of e^-p. Comparison between the two provides tests of factorization, and detailed studies of the proton initial state (*e.g.* TMDs, structure functions). e^-p provides a natural intermediate step between e^+e^- and pp. Furthermore, EEC has a number of good unique theoretical properties, so it can be computed to high accuracy [50–53] and has suppressed non-perturbative effects through energy weighting. This has enabled an α_s extraction with record precision using jet substructure method in pp [54]. It is interesting to explore if it will make a competitive α_s extraction in a different system. Additionally, the EEC can be expanded for the study of spin effects in a polarized target hadron and therefore, constitutes a useful tool for the study TMD physics and nuclear matter effects at the future Electron Ion Collider (EIC) [40].

The observable $\mathrm{EEC}_{\mathrm{DIS}}$ is defined as

$$\mathrm{EEC}_{\mathrm{DIS}} = \sum_a \int \frac{\mathrm{d}\sigma_{ep\to e+a+X}}{\sigma} \, z_a \, \delta(\cos\theta_{ap} - \cos\theta) \,, \tag{7}$$

where

$$z_a \equiv \frac{P \cdot p_q}{P \cdot (\sum_i p_i)} \,, \tag{8}$$

and p_a^μ and P^μ are the momenta of the hadron a and the incoming proton respectively. The angle θ_{ap} is the polar angle of hadron a, which is measured with respect to the incoming proton. The asymmetric weight function, z_a, is suppressed for soft radiation and radiation close to the beam direction. In this analysis, we calculate the $\mathrm{EEC}_{\mathrm{DIS}}$ observable by looping over hadrons and calculate z_a and the angle θ_{ap} with respect to the proton. Furthermore, this definition of $\mathrm{EEC}_{\mathrm{DIS}}$ naturally separates the contribution to the $\cos\theta$ spectrum from: (a) wide angle soft radiation, (b) initial state radiation and beam remnants, and (c) radiation from the hadronization of the struck quark [40].

3 Monte Carlo simulations

Monte Carlo (MC) simulations are used to correct the data for detector acceptance and resolution effects as well as to compare theoretical predictions with experimental results.

Detector acceptance and resolution effects are estimated using the Djangoh 1.4 [55] and Rapgap 3.1 [56] simulators. Both generators implement Born level matrix elements for neutral current DIS, boson–gluon fusion, and QCD Compton processes and are interfaced with HERACLES [57–59] for QED radiation. The CTEQ6L PDF set [60] and the Lund hadronization model [61] with parameters determined by the ALEPH Collaboration [62] are used for the non-perturbative components. Djangoh uses the Color Dipole Model as implemented in ARIADNE [63] for higher order emissions, and Rapgap uses parton showers in the leading logarithmic approximation. Each of these generators is combined with a detailed simulation of the H1 detector response based on GEANT3 [64] and the generated events are reconstructed in the same way as data. The same selection described in 2 is applied to Particle-level event and particle simulation. Reco-level MC events and particles have a more relaxed selection applied, requiring the event

have $Q^2 > 100$ GeV^2 and at least one particle reconstructed in the event. Particle-level MC events with $Q^2 > 150$ GeV^2, $0.08 < y < 0.7$ and particles with $p_{\mathrm{T}}^{\mathrm{part}} > 0.1$ GeV and $-1.5 < \eta^{\mathrm{part.}} < 2.75$ are selected. Additionally, MC events with no particles passing this selection are rejected before the unfolding.

4 Unfolding

The unfolding procedure for this measurement, OMNIFOLD [13,14], is used for the unbinned unfolding of all particles. While in all previous measurements a subset of observables were used for unfolding, this time we aim to include the entire event information. The OMNIFOLD method is an iterative two-step (expectation-maximization) procedure to correct for detector effects. The goal is to infer particle-level data using detector-level data and simulations. The main components of OMNIFOLD are explained in more detail below.

The inputs to the unfolding are:

- Per-particles features: $[p_{\mathrm{T}},\ \eta,\ \phi,\ C\ ]$
- Global DIS quantities: $[Q^2,\ y,\ p_x^e,\ p_y^e,\ p_z^e]$,

with $p_{\mathrm{T}},\ \eta,\ \phi,\ C$ as the particles' transverse momentum, pseudorapidity, azimuthal angle, and electric charge, respectively. The momenta p_x^e, p_y^e, and p_z^e are the $\hat{x}, \hat{y}$, and $\hat{z}$ component of the scattered lepton momentum in Cartesian coordinates. Lastly, Q^2 and y are the transverse momentum square and inelasticity of the event. These features, $[p_{\mathrm{T}},\ \eta,\ \phi,\ C\ ]$ and $[Q^2,\ y,\ p_x^e,\ p_y^e,\ p_z^e]$, are represented as the input vector $\vec{x}$ in the description of the unfolding procedure.

The first step of OMNIFOLD uses observables at detector level while the second step operates at particle level. Let $X_{\mathrm{data}} = \{\vec{x}_i\}$ be the set of events in data and $X_{\mathrm{MC,gen}} = \{\vec{x}_{\mathrm{gen},i}\}$ and $X_{\mathrm{MC,reco}} = \{\vec{x}_{\mathrm{reco},i}\}$ be sets of events in simulation with a correspondence between the two sets. In simulation, there is a set of observables at particle-level and detector-level for each event. If an event does not pass the particle-level or detector-level event selection, then the observables for that event are assigned a dummy value $\vec{x} = \emptyset$. Each event i in simulation is also associated with a weight w_i from the MC simulation.

OMNIFOLD achieves an unbinned unfolding by iteratively re-weighting the particle-level events. Each event i in simulation is given a weight ν_i and these weights are updated at each iteration. The final result is the simulated events with weights $\nu_i w_i$. From these events, one can compute new observables defined on $\vec{x}$ and can construct histograms or other summary statistics. The OMNIFOLD weights are initialized at $\nu_i = 1$, i.e. the prior is the initial MC simulation.

The first step of OMNIFOLD is to train a classifier f to distinguish the weighted simulation at detector-level from the data. The classifier is trained to maximize the common binary cross entropy:

$$\varepsilon = \sum_{\vec{x}_i \in X_{\mathrm{data}}} \log(f(\vec{x}_i)) + \sum_{\vec{x}_i \in X_{\mathrm{MC,reco}}} \nu_i w_i \log(1 - f(\vec{x}_i)), \tag{9}$$

where both sums only include events that pass the detector-level selection. For events that pass the detector-level selection, define $\lambda_i = \nu_i \cdot f(\vec{x}_i)/(1 - f(\vec{x}_i))$ for $\vec{x}_i \in X_{\mathrm{MC,reco}}$. This manipulation of the classifier output is known (see e.g. Refs. [65–67]) to produce an estimate of the ratio of the likelihoods for the event to be from the measured data or from the simulation. For events that do not pass the detector-level selection, $\lambda_i = \nu_i$.

The second step of OMNIFOLD is a regularization step. The weights λ_i are insufficient because they are not a proper function of the particle-level phase space. In other words, a single phase space point

$\vec{x}_{\text{gen}}$ can be mapped to different $\vec{x}_{\text{reco}}$ values under the stochastic detector response. The second step of OMNIFOLD averages the weights λ for a fixed particle-level phase space point. This is accomplished by training a classifier to distinguish the particle-level simulation weighted by ν from the particle-level simulation weighted by λ. The loss function is once again the binary cross entropy:

$$L = \sum_{\vec{x}_i \in X_{\text{MC,truth}}} \lambda_i w_i \log(f'(\vec{x}_i)) + \nu_i w_i \log(1 - f'(\vec{x}_i)), \tag{10}$$

where the sum only includes events that pass the particle-level selection. For events that pass the particle-level selection, define $\nu_{i+1} = \nu_i \cdot f(\vec{x}_i)/(1 - f(\vec{x}_i))$ for $\vec{x}_i \in X_{\text{MC,truth}}$. For events that do not pass the particle-level selection, ν_i is left unchanged from its previous value.

The classifiers for Steps 1 and 2 are parameterized as neural networks. In order to process all the particles and lepton information in the event we use an adapted version of the OMNILEARN model [15, 16]. The OMNILEARN model combines the scalability of transformer models using the point-edge transformer architecture and encodes the local information using graph neural networks. More specifically, a local embedding is created for each hadron using the k-nearest neighbors of each particle in $\eta - \phi$ space, where k is set to 5. The representation of each hadron is then updated based on the local embedding information and used as an input for four transformer layers. The classification output is encoded using a classification token [68]. The classification token summarizes the information of the entire point cloud and returns a binary output used for the classification task. All hyperparameters of the model, including number of layers, number off neighbors, and layer sizes were optimized by running multiple trainings and tracking the value of the validation loss of the classification between the Rapgap and Djangoh simulations. Since the entire procedure is computationally expensive, we only considered options that lead to acceptable running times, but we did check that using more complex models did not lead to noticeable improvements in the validation loss. All networks are implemented in TENSORFLOW [69] and KERAS [70] and optimized using LION [71]. All inputs are scaled so that each input feature has mean zero and unit standard deviation.

In previous measurements with OMNIFOLD, each training would start from a network initialized using random weights. Since the size of the simulated samples are 2 orders of magnitude bigger than the data, the unfolding precision was limited by the data size. We can improve the quality and stability of the unfolding procedure by first pre-training a model to fulfill a specific task, in this case, the classification between Rapgap and Djangoh simulations. For this task, we use 20M Rapgap and 20M Djangoh events. This pre-trained model can then be used as the starting point for the unfolding procedure of all subsequent unfolding runs. The validation loss obtained by using the pre-trained model on the first OMNIFOLD iteration is compared with the loss observed by training a model from scratch in Fig. 2.

5 Uncertainties

Systematic uncertainties on the description of the detector are estimated by varying the relevant aspects of the simulation and carrying out the full analysis procedure with the varied simulation set. We include the systematic uncertainties related to the modeling of reconstructed hadrons and scattered lepton. In particular, the energy scale and azimuthal angle are carefully considered. The uncertainties on the HFS energy scale are categorized into two classifications: HFS objects within high p_{T} jets and all other remaining HFS objects. The energy-scale uncertainty in both cases is $\pm 1\%$. Both sources of uncertainty are estimated separately [72, 73] by varying each HFS energy by $\pm 1\%$. An uncertainty of ± 20 mrad is assigned to the azimuthal angle determination of HFS objects. The uncertainties on the lepton energy scale ranges from $\pm 0.5\%$ to $\pm 1\%$ [73, 74]. Uncertainties on the azimuthal angle of the scattered lepton are estimated to be ± 1 mrad [75]. For each variation to the simulation, the models for the unfolding are completely retrained and the unfolding procedure is repeated. The full difference in the final observable from the nominal result is taken as the uncertainty for that variation.

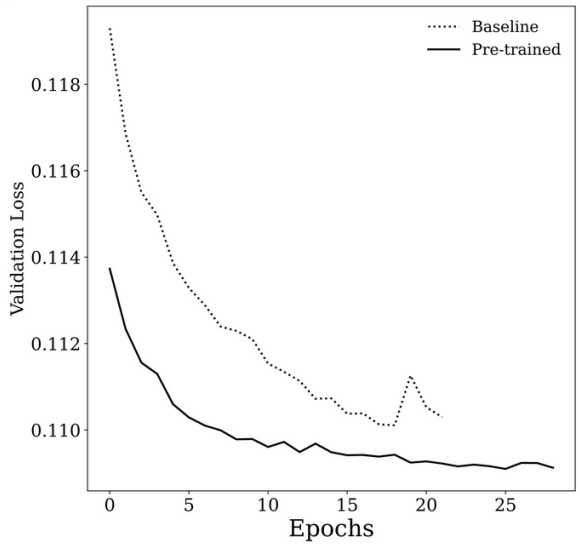

Fig. 2: Comparison of the validation loss obtained by training the first step and iteration of OMNIFOLD either using a model initialized with random weights (dotted lines) and a model initialized using the same weights of the pre-training task (full lines).

QED corrections are not yet included in the current analysis.

We include two types of unfolding uncertainties to the final results. The first one is determined from a closure test, where the Rapgap simulation is used to unfold the response of the Djangoh simulation. In this setting, we restrict the number of events in the Djangoh simulation to match the one expected from the data. The difference between the unfolded results and the true response from Djangoh is used as an uncertainty. An additional uncertainty from the unfolding procedure is estimated to cover a possible bias from the generator choice used to perform the unfolding. This is designated as the model bias, and is estimated by the difference in results obtained when performing the unfolding with the Rapgap or Djangoh simulations.

The statistical uncertainty of the measurement is estimated using the bootstrap technique [76]. The unfolding procedure is repeated on 25 pseudo datasets, each defined by resampling the original data according to a Poisson distribution with $\mu = 1$. The number of MC events exceeds the number of data events by nearly two orders of magnitude and therefore the MC statistical uncertainty is negligible compared to the corresponding data uncertainty. Variations from the random nature of the network initialization and training are negligible compared to the data statistical uncertainty.

6 Results

6.1 Closure results

Before looking at the unfolded data, a closure test is performed to validate the unfolding procedure. The closure unfolding procedure is done with Rapgap as the Monte Carlo simulation and Djangoh as pseudodata. Figures 3, 4, 5, 6, and 7 show the closure results for the observables discussed in Sec. 2. All of the unfolded observables show good agreement with the truth Djangoh values. The remaining differences between the unfolded distributions and Djangoh predictions are used as an uncertainty.

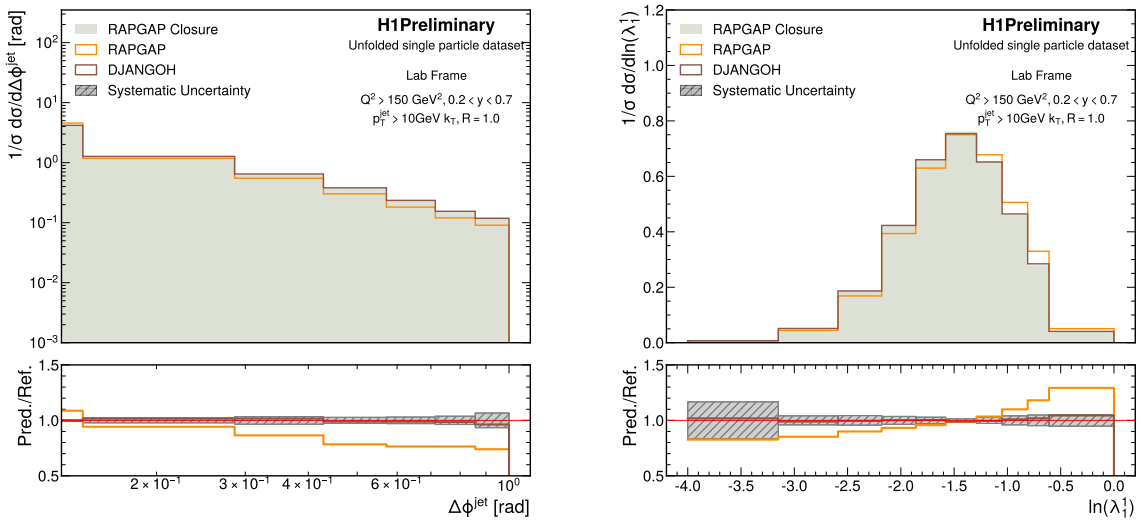

Fig. 3: Closure test of $\Delta\phi^{\text{jet}}$ (left) and $\ln(\lambda_1^1)$ (right) in the laboratory frame using the k_{T} algorithm with $R = 1$. These plots contain jets with $p_{\text{T}}^{\text{jet}} > 10$ GeV. The RAPGAP and DJANGOH data are at the generation-level. The RAPGAP Closure histogram is the RAPGAP results with unfolded weights applied. Ref. in the bottom panel is RAPGAP Closure.

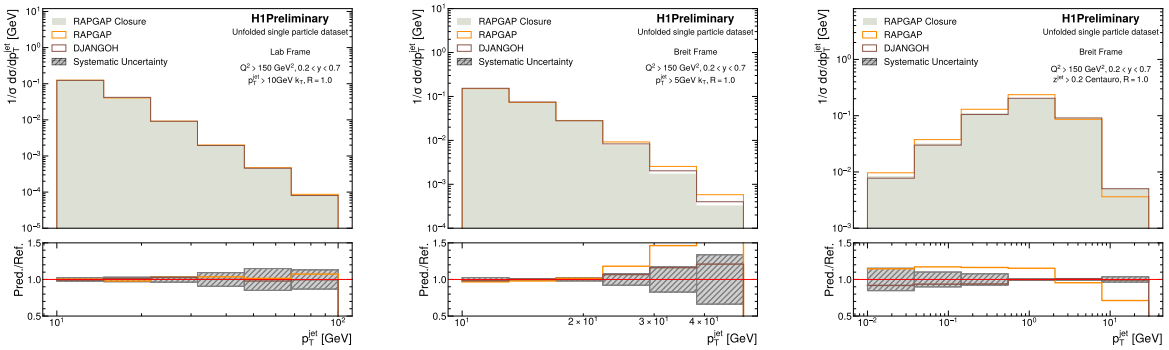

Fig. 4: Closure test of $p_{\text{T}}^{\text{jet}}$ in the laboratory frame (left) and Breit frame (middle) using the k_{T} algorithm and in the Breit frame using the Centauro algorithm (right). These all use $R = 1$. The laboratory k_{T}, Breit k_{T}, and Breit Centauro plots use a $p_{\text{T}}^{\text{jet}} > 10$ GeV cut, a $p_{\text{T}}^{\text{jet}} > 5$ GeV cut, and a $z^{\text{jet}} > 0.2$ cut, respectively. The RAPGAP and DJANGOH data are at the generation-level. The RAPGAP Closure histogram is the RAPGAP results with unfolded weights applied. Ref. in the bottom panel is RAPGAP Closure.

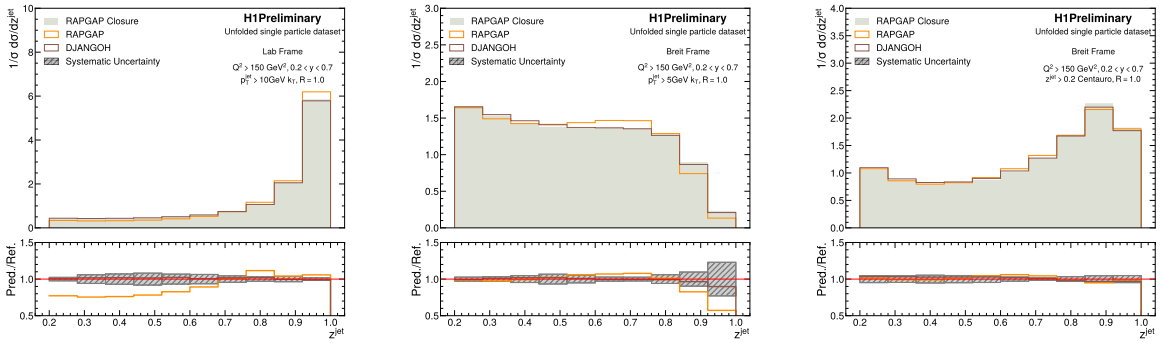

Fig. 5: Closure test of z^{jet} in the laboratory frame (left) and Breit frame (middle) using the k_{T} algorithm and in the Breit frame using the Centauro algorithm (right). These all use $R = 1$. The laboratory k_{T}, Breit k_{T}, and Centauro plots use a $p_{\text{T}}^{\text{jet}} > 10$ GeV cut, a $p_{\text{T}}^{\text{jet}} > 5$ GeV cut, and a $z^{\text{jet}} > 0.2$ cut, respectively. The RAPGAP and DJANGOH data are at the generation-level. The RAPGAP Closure histogram is the RAPGAP results with unfolded weights applied. Ref. in the bottom panel is RAPGAP Closure.

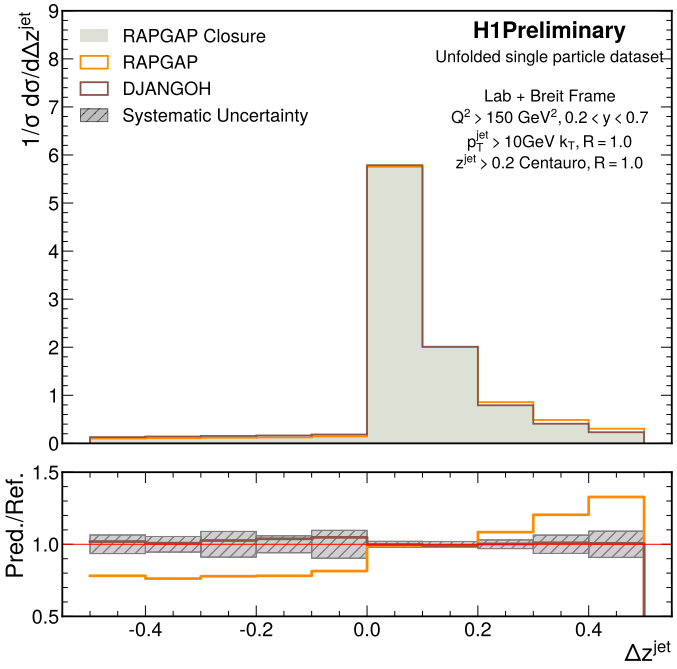

Fig. 6: Closure test of Δz^{jet}. Δz^{jet} is defined as in Equation 6, where the values of z^{jet} from the leading jets clustered from k_{T} and Centauro are subtracted. The RAPGAP and DJANGOH data are at the generation-level. The RAPGAP Closure histogram is the RAPGAP results with unfolded weights applied. Ref. in the bottom panel is RAPGAP Closure.

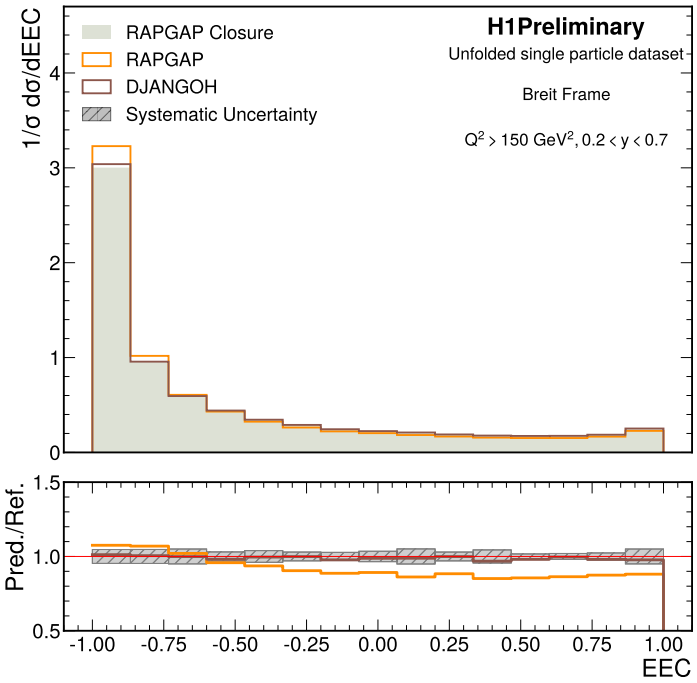

Fig. 7: Closure test of $\mathrm{EEC_{DIS}}$. $\mathrm{EEC_{DIS}}$ is defined as in Eq. 7 and calculated using all the particles with $p_T^{\mathrm{part}} > 100$ MeV in Breit frame. The RAPGAP and DJANGOH histograms are at generation-level. The RAPGAP Closure histogram is the result with the unfolded weights applied. The bottom panel shows the ratio of the unfolding closure to the initial RAPGAP data and the targeted DJANGOH data.

6.2 Unfolded Results

Finally, we show the unfolding results obtained in this analysis, in Figures 8, 9, 10, 11, and 12. In these plots, the unfolded results and the two Monte Carlo datasets are shown. The ratio to the unfolded results is displayed in the bottom panel.

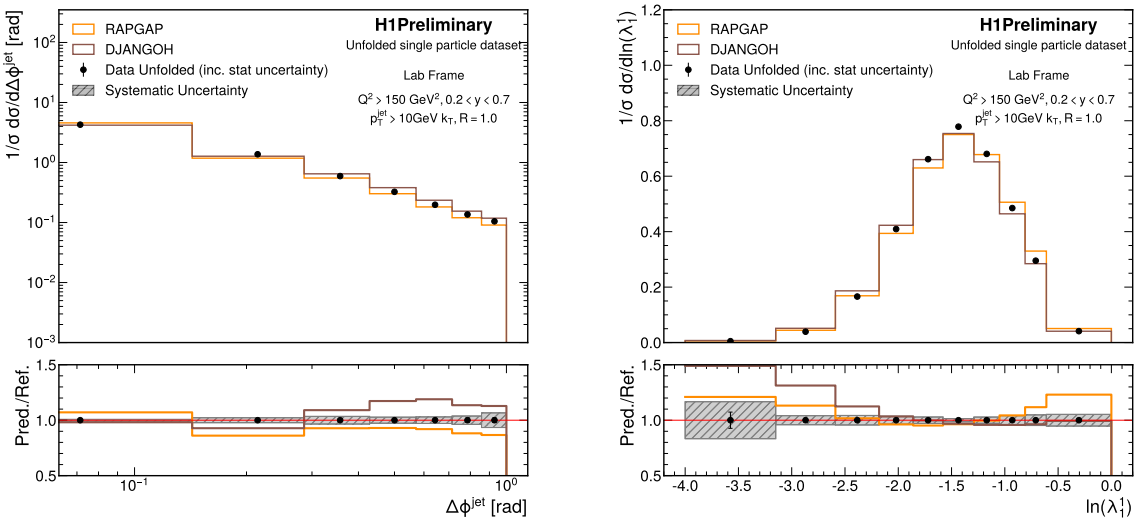

Fig. 8: Unfolded $\Delta\phi^{\text{jet}}$ (left) and $\ln(\lambda_1^1)$ (right) in the laboratory frame using the k_T algorithm with $R = 1$. These plots contain jets with $p_T^{\text{jet}} > 10$ GeV. The RAPGAP and DJANGOH data are at the generation-level. Data Unfolded is the unfolded H1 data. Ref. in the bottom panel is the unfolded data.

The distributions of $\Delta\phi^{\text{jet}}$ and $\ln(\lambda_1^1)$ in Fig. 9 qualitatively agree with previous published results shown in Refs. [3, 5], where at smaller values of $\Delta\phi^{\text{jet}}$, the DJANGOH simulation agrees with the measured value, but at higher values both simulations start to show discrepancies compared to the measured values. Similarly, the jet girth shows an agreement with predictions at the peak value of the distribution but starts to show deviations near the tails of the distribution.

The peak around unity in the left panel of Figure 10 originates from DIS events with configurations close to the Born level. In these events, a high-p_T jet balances the high-p_T electron by taking most of the energy of the struck quark. In the Breit frame, this peak is removed by applying a minimum $p_T > 5$ GeV requirement. This cut effectively excludes DIS events close to the Born-level configuration and instead selects events with dijet or multijet configurations arising from higher-order processes, such as photon-gluon fusion. The minimum p_T is necessary; otherwise, the k_T algorithm would yield pathological results, such as a high multiplicity of jets with low p_T.

The Centauro jet measurements in the right panel of Figure 10 show a peak near unity, as expected since, in the Breit frame, the Centauro algorithm can cluster the leading jet in DIS events with configurations close to the Born level—unlike the k_T algorithm. The Centauro jet p_T spectrum exhibits a peak around 1 GeV. This peaking behavior is qualitatively similar to our previous measurement [3] of the q_T distribution in the laboratory frame using the k_T algorithm, which plays an analogous role to the jet p_T in the Breit frame. Both observables are expected to be sensitive to quark transverse-momentum-dependent (TMD) PDFs, see Ref. [77] for a discussion on Centauro algorithm, and Ref. [78] for discussion of q_T in the laboratory frame.

The Centauro jet z peak, however, is observed to be significantly broader than the corresponding peak in laboratory-frame measurements. To further quantify this difference, we compare the z values between

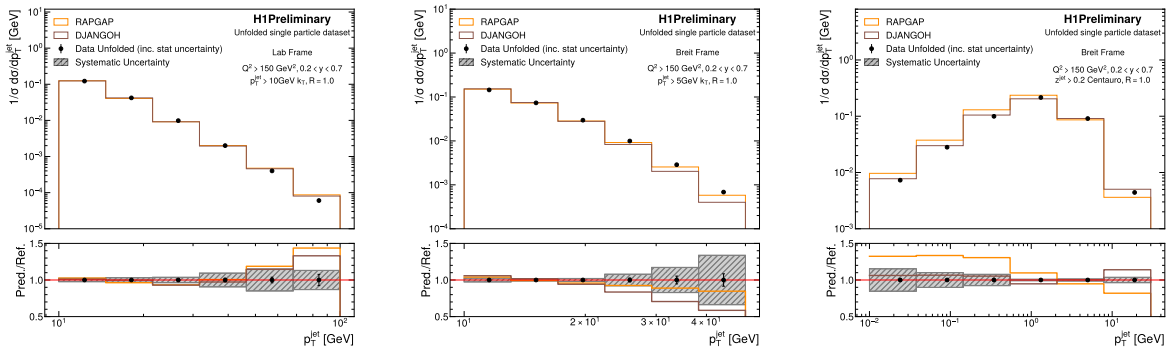

Fig. 9: Unfolded $p_{\mathrm{T}}^{\mathrm{jet}}$ in the laboratory frame (left) and Breit frame (middle) using the k_{T} algorithm and in the Breit frame using the Centauro algorithm (right). These all use $R = 1$. The laboratory k_{T}, Breit k_{T}, and Centauro plots use a $p_{\mathrm{T}}^{\mathrm{jet}} > 10$ GeV cut, a $p_{\mathrm{T}}^{\mathrm{jet}} > 5$ GeV cut, and a $z^{\mathrm{jet}} > 0.2$ cut, respectively. The RAPGAP and DJANGOH data are at the generation-level. Data Unfolded is the unfolded H1 data. Ref. in the bottom panel is the unfolded data.

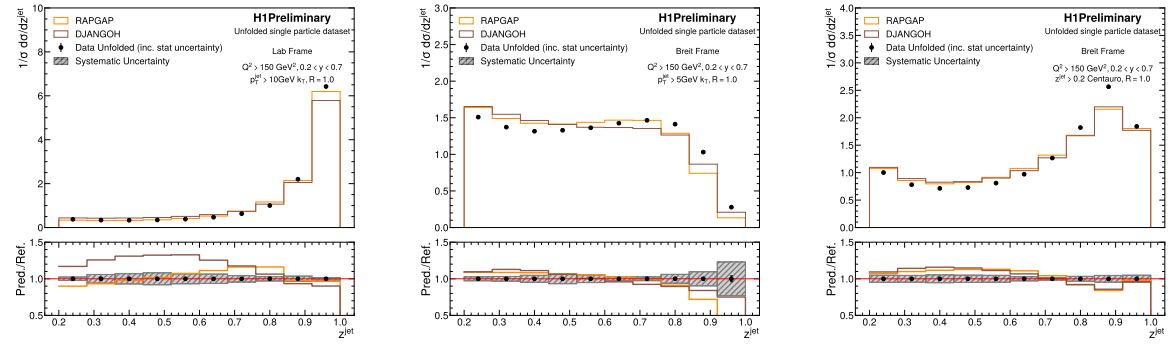

Fig. 10: Unfolded z^{jet} in the laboratory frame (left) and Breit frame (middle) using the k_{T} algorithm and in the Breit frame using the Centauro algorithm (right). These all use $R = 1$. The laboratory k_{T}, Breit k_{T}, and Centauro plots use a $p_{\mathrm{T}}^{\mathrm{jet}} > 10$ GeV cut, a $p_{\mathrm{T}}^{\mathrm{jet}} > 5$ GeV cut, and a $z^{\mathrm{jet}} > 0.2$ cut, respectively. The RAPGAP and DJANGOH data are at the generation-level. Data Unfolded is the unfolded H1 data. Ref. in the bottom panel is the unfolded data.

the leading jets clustered in the laboratory frame and the leading Centauro jets in the Breit frame, The leading jets are those with the highest z^{jet} values. Note that such a measurement is only possible when events are analyzed simultaneously in both the laboratory and Breit frames, which is feasible with the current unfolding approach.

The Δz^{jet} distribution peaks at zero and exhibits two asymmetric tails, with the positive tail being significantly more prominent. This may suggest that clustering jets in the laboratory frame captures a greater fraction of the struck quark's energy than clustering in the Breit frame. However, the distribution could also be affected by QED radiation, which influences the boost to the Breit frame. QED radiation effects are not corrected at this stage of the analysis.

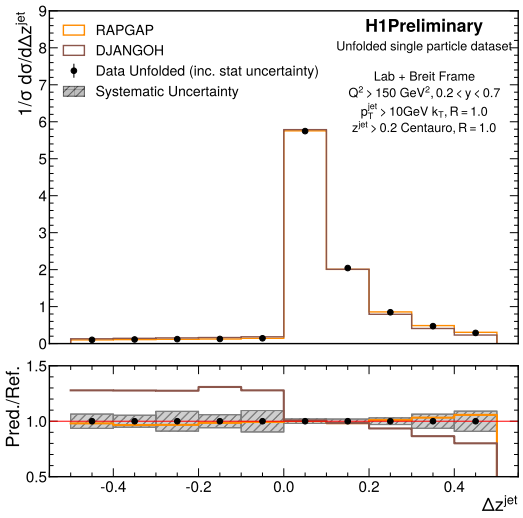

Fig. 11: Unfolded Δz^{jet}. Δz^{jet} is defined as in Equation 6, where the values of z^{jet} from the leading jets clustered from k_{T} and Centauro are subtracted. The RAPGAP and DJANGOH data are at the generation-level. Data Unfolded is the unfolded H1 data. Ref. in the bottom panel is the unfolded data.

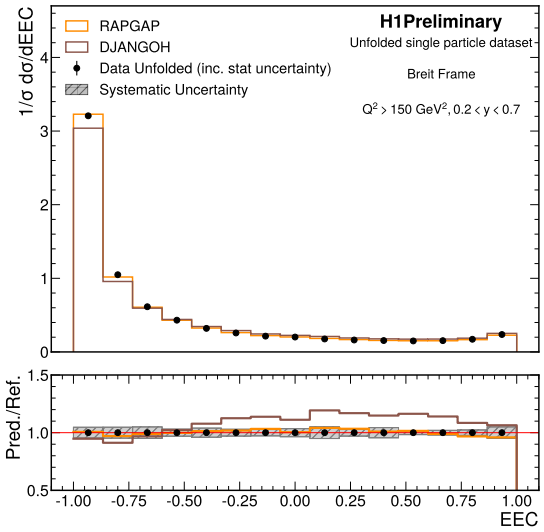

Fig. 12: Unfolded EEC_{DIS}. EEC_{DIS} is defined as in in Equation 7 and calculated using all the particles with $p_T^{\text{part}} > 100$ MeV in Breit frame. More details may be found in Ref. [40]. The RAPGAP and DJANGOH histograms are at the generation-level. The 'Data Unfolded' histogram is the unfolded H1 data. Ref. in the bottom panel is the unfolded data.

7 Conclusions and Outlook

This work presents the first complete implementation of OMNIFOLD used to unfold all particles in DIS events measured with the H1 detector. Unfolding all particles in the events has enabled for the first time many impactful studies; the first measurement of EEC_{DIS} in Breit frame is presented, as well as a comparison of Jets in both the Center-of-Mass and Breit frames.

The first study comparing of jets clustered in the laboratory and Breit frames, using the k_T and Centauro algorithms, respectively, indicate significant differences in the resulting z distribution, which is intended to be a Lorentz invariant reflecting the energy fraction of the struck quark carried by the jet. These differences suggest that the choice of clustering algorithm plays an important role in the analysis of this variable, an effect not expected at leading order. However, this interpretation is tempered by the fact that QED radiation—which has not been corrected for at this stage—is also expected to affect the z distributions differently in the laboratory and Breit frames, with the latter being more sensitive due to the required boost.

8 Acknowledgments

We would like to thank Kyle Lee and Ian Moult for the very helpful discussions and advice. This material is based upon work supported by the National Science Foundation under Grant No. 2311666. We express our thanks to all those involved in securing not only the H1 data but also the software and working environment for long term use, allowing the unique H1 data set to continue to be explored. The transfer from experiment specific to central resources with long term support, including both storage and batch systems, has also been crucial to this enterprise. We therefore also acknowledge the role played by DESY-IT and all people involved during this transition and their future role in the years to come.

References

[1] C. Diaconu, T. Haas, M. Medinnis, K. Rith, and A. Wagner. Physics accomplishments of hera. *Annual Review of Nuclear and Particle Science*, 60(Volume 60, 2010):101–128, 2010.

[2] Miguel Arratia et al. Presenting Unbinned Differential Cross Section Results. *JINST*, 17 P01024, 1 2022.

[3] Andreev, V. and others. Measurement of Lepton-Jet Correlation in Deep-Inelastic Scattering with the H1 Detector Using Machine Learning for Unfolding. *Phys. Rev. Lett.*, 128:132002, Mar 2022.

[4] H1 Collaboration. Machine learning-assisted measurement of multi-differential lepton-jet correlations in deep-inelastic scattering with the H1 detector. *H1prelim-22-031*, 2022.

[5] V. Andreev et al. Unbinned deep learning jet substructure measurement in high Q2 ep collisions at HERA. *Physics Letters B*, 844:138101, 2023.

[6] V. Andreev et al. Machine Learning-Assisted Measurement of Lepton-Jet Azimuthal Angular Asymmetries in Deep-Inelastic Scattering at HERA. 12 2024.

[7] R. Aaij et al. Multidifferential study of identified charged hadron distributions in Z-tagged jets in proton-proton collisions at $\sqrt{s} = 13$TeV. *Phys. Rev. D*, 108:L031103, Aug 2023.

[8] Youqi Song. Measurement of CollinearDrop jet mass and its correlation with SoftDrop groomed jet substructure observables in $\sqrt{s} = 200$ GeV pp collisions by STAR. 7 2023.

[9] Tanmay Pani. Generalized angularities measurements from STAR at $\sqrt$SNN = 200 GeV. *EPJ Web Conf.*, 296:11003, 2024.

[10] G. Aad et al. Simultaneous Unbinned Differential Cross-Section Measurement of Twenty-Four $Z+$jets Kinematic Observables with the ATLAS Detector. *Phys. Rev. Lett.*, 133:261803, Dec 2024.

[11] Georges Aad et al. Measurement of jet track functions in pp collisions at $\sqrt{s} = 13$ TeV with the ATLAS detector. 2 2025.

[12] Measurement of event shapes in minimum bias events from pp collisions at 13 TeV. Technical report, CERN, Geneva, 2024.

[13] Anders Andreassen, Patrick T. Komiske, Eric M. Metodiev, Benjamin Nachman, and Jesse Thaler. OmniFold: A Method to Simultaneously Unfold All Observables. *Phys. Rev. Lett.*, 124(18):182001, 2020.

[14] Anders Andreassen, Patrick T. Komiske, Eric M. Metodiev, Benjamin Nachman, Adi Suresh, and Jesse Thaler. Scaffolding Simulations witih Deep Learning for High-Dimensional Deconvolution. *ICLR SimDL Workshop*, page 12, 2021.

[15] Vinicius Mikuni and Benjamin Nachman. Solving Key Challenges in Collider Physics with Foundation Models. 4 2024.

[16] Vinicius Mikuni and Benjamin Nachman. A Method to Simultaneously Facilitate All Jet Physics Tasks. 2 2025.

[17] I. Abt et al. The H1 detector at HERA. *DESY-93-103*, 7 1993.

[18] B. Andrieu et al. The H1 liquid argon calorimeter system. *Nucl. Instrum. Meth. A*, 336:460–498, 1993.

[19] I. Abt et al. The H1 detector at HERA. *Nucl. Instrum. Meth. A*, 386:310–347, 1997.

[20] I. Abt et al. The Tracking, calorimeter and muon detectors of the H1 experiment at HERA. *Nucl. Instrum. Meth. A*, 386:348–396, 1997.

[21] R. D. Appuhn et al. The H1 lead / scintillating fiber calorimeter. *Nucl. Instrum. Meth. A*, 386:397–408, 1997.

[22] D. Pitzl et al. The H1 silicon vertex detector. *Nucl. Instrum. Meth. A*, 454:334–349, 2000.

[23] B. Andrieu et al. Beam tests and calibration of the H1 liquid argon calorimeter with electrons. *Nucl. Instrum. Meth. A*, 350:57–72, 1994.

[24] B. Andrieu et al. Results from pion calibration runs for the H1 liquid argon calorimeter and comparisons with simulations. *Nucl. Instrum. Meth. A*, 336:499–509, 1993.

[25] F. D. Aaron et al. Determination of the Integrated Luminosity at HERA using Elastic QED Compton Events. *Eur. Phys. J. C*, 72:2163, 2012. [Erratum: Eur.Phys.J.C 74, 2733 (2014)].

[26] Ursula Bassler and Gregorio Bernardi. On the kinematic reconstruction of deep inelastic scattering at HERA: The Sigma method. *Nucl. Instrum. Meth. A*, 361:197–208, 1995.

[27] C. Adloff et al. Measurement and QCD analysis of neutral and charged current cross-sections at HERA. *Eur. Phys. J. C*, 30:1–32, 2003.

[28] F. D. Aaron et al. Inclusive Deep Inelastic Scattering at High Q^2 with Longitudinally Polarised Lepton Beams at HERA. *JHEP*, 09:061, 2012.

[29] V. Andreev et al. Measurement of multijet production in ep collisions at high Q^2 and determination of the strong coupling α_s. *Eur. Phys. J. C*, 75(2):65, 2015.

[30] V. Andreev et al. Measurement of Jet Production Cross Sections in Deep-inelastic ep Scattering at HERA. *Eur. Phys. J. C*, 77(4):215, 2017. [Erratum: Eur.Phys.J.C 81, 739 (2021)].

[31] Matteo Cacciari, Gavin P. Salam, and Gregory Soyez. FastJet User Manual. *Eur. Phys. J. C*, 72:1896, 2012.

[32] Matteo Cacciari and Gavin P. Salam. Dispelling the N^3 myth for the k_t jet-finder. *Phys. Lett. B*, 641:57–61, 2006.

[33] S. Catani, Yuri L. Dokshitzer, M. H. Seymour, and B. R. Webber. Longitudinally invariant K_t clustering algorithms for hadron hadron collisions. *Nucl. Phys. B*, 406:187–224, 1993.

[34] Stephen D. Ellis and Davison E. Soper. Successive combination jet algorithm for hadron collisions. *Phys. Rev. D*, 48:3160–3166, 1993.

[35] Matti Peez. Search for deviations from the standard model in high transverse energy processes at the electron proton collider HERA, 10 2003.

[36] S Hellwig. Untersuchung der D^* - π slow Double Tagging Methode in Charmanalysen. (Diploma, Univ. Hamburg), 2005.

[37] B Portheault. First measurement of charged and neutral current cross sections with the polarized positron beam at HERA II and QCD-electroweak analyses. (Thesis, Univ. Paris XI), 2005.

[38] V. Andreev et al. Observation and differential cross section measurement of neutral current DIS events with an empty hemisphere in the Breit frame. *Eur. Phys. J. C*, 84, 7 2024.

[39] M. Arratia, Y. Makris, D. Neill, F. Ringer, and N. Sato. Asymmetric jet clustering in deep-inelastic scattering. *Phys. Rev. D*, 104:034005, 8 2021.

[40] Hai Tao Li, Yiannis Makris, and Ivan Vitev. Energy-energy correlators in deep inelastic scattering. *Physical Review D*, 103(9), May 2021.

[41] Diego M Hofman and Juan Maldacena. Conformal collider physics: energy and charge correlations. *Journal of High Energy Physics*, 2008(05):012–012, may 2008.

[42] Carlota Andres, Fabio Dominguez, Raghav Kunnawalkam Elayavalli, Jack Holguin, Cyrille Marquet, and Ian Moult. Resolving the Scales of the Quark-Gluon Plasma with Energy Correlators. 9 2022.

[43] Evan Craft, Kyle Lee, Bianka Meçaj, and Ian Moult. Beautiful and Charming Energy Correlators. 10 2022.

[44] Jack Holguin, Ian Moult, Aditya Pathak, Massimiliano Procura, Robert Schöfbeck, and Dennis Schwarz. Using the W as a Standard Candle to Reach the Top: Calibrating Energy Correlator Based Top Mass Measurements. 11 2023.

[45] Hannah Bossi, Arjun Srinivasan Kudinoor, Ian Moult, Daniel Pablos, Ananya Rai, and Krishna Rajagopal. Imaging the Wakes of Jets with Energy-Energy-Energy Correlators. 7 2024.

[46] Xiaohui Liu and Hua Xing Zhu. Nucleon Energy Correlators. *Phys. Rev. Lett.*, 130(9):091901,

2023.

[47] Hao-Yu Liu, Xiaohui Liu, Ji-Chen Pan, Feng Yuan, and Hua Xing Zhu. Nucleon Energy Correlators for the Color Glass Condensate. *Phys. Rev. Lett.*, 130(18):181901, 2023.

[48] Haotian Cao, Hai Tao Li, and Zihao Mi. Bjorken x weighted energy-energy correlators from the target fragmentation region to the current fragmentation region. *Phys. Rev. D*, 109(9):096004, 2024.

[49] Hannah Bossi, Austin Baty, Yi Chen, Yu-Chen Chen, Gian-Michele Innocenti, Marcello Maggi, Chris McGinn, and Yen-Jie Lee. Measurement of the energy-energy correlator in the back-to-back limit using the archived ALEPH e^+e^- data at 91.2 GeV, 2025.

[50] Lance J. Dixon, Ming-Xing Luo, Vladyslav Shtabovenko, Tong-Zhi Yang, and Hua Xing Zhu. Analytical Computation of Energy-Energy Correlation at Next-to-Leading Order in QCD. *Phys. Rev. Lett.*, 120(10):102001, 2018.

[51] Lance J. Dixon, Ian Moult, and Hua Xing Zhu. Collinear limit of the energy-energy correlator. *Phys. Rev. D*, 100(1):014009, 2019.

[52] Claude Duhr, Bernhard Mistlberger, and Gherardo Vita. Four-Loop Rapidity Anomalous Dimension and Event Shapes to Fourth Logarithmic Order. *Phys. Rev. Lett.*, 129(16):162001, 2022.

[53] Wen Chen, Jun Gao, Yibei Li, Zhen Xu, Xiaoyuan Zhang, and Hua Xing Zhu. NNLL Resummation for Projected Three-Point Energy Correlator. 7 2023.

[54] Aram Hayrapetyan et al. Measurement of energy correlators inside jets and determination of the strong coupling $\alpha_S(m_Z)$. 2 2024.

[55] K. Charchula, G. A. Schuler, and H. Spiesberger. Combined QED and QCD radiative effects in deep inelastic lepton - proton scattering: The Monte Carlo generator DJANGO6. *Comput. Phys. Commun.*, 81:381–402, 1994.

[56] Hannes Jung. Hard diffractive scattering in high-energy e p collisions and the Monte Carlo generator RAPGAP. *Comput. Phys. Commun.*, 86:147–161, 1995.

[57] H. Spiesberger et al. Radiative corrections at HERA. In *Workshop on Physics at HERA*, 3 1992.

[58] A Kwiatkowski, H. Spiesberger, and H. J. Mohring. Characteristics of radiative events in deep inelastic e p scattering at HERA. *Z. Phys. C*, 50:165–178, 1991.

[59] A. Kwiatkowski, H. Spiesberger, and H. J. Mohring. Heracles: An Event Generator for *ep* Interactions at HERA Energies Including Radiative Processes: Version 1.0. *Comput. Phys. Commun.*, 69:155–172, 1992.

[60] J. Pumplin, D. R. Stump, J. Huston, H. L. Lai, Pavel M. Nadolsky, and W. K. Tung. New generation of parton distributions with uncertainties from global QCD analysis. *JHEP*, 07:012, 2002.

[61] B. Andersson, G. Gustafson, G. Ingelman, and T. Sjöstrand. Parton fragmentation and string dynamics. *Phys. Rept.*, 97:31–145, 1983.

[62] S. Schael et al. Bose-Einstein correlations in W-pair decays with an event-mixing technique. *Phys. Lett. B*, 606:265–275, 2005.

[63] L. Lönnblad. ARIADNE version 4: A Program for simulation of QCD cascades implementing the color dipole model. *Comput. Phys. Commun.*, 71:15–31, 1992.

[64] R. Brun, F. Bruyant, M. Maire, A. C. McPherson, and P. Zanarini. GEANT3. *CERN-DD-EE-84-01*, 9 1987.

[65] Trevor Hastie, Robert Tibshirani, and Jerome Friedman. *The Elements of Statistical Learning*. Springer Series in Statistics. Springer New York Inc., New York, NY, USA, 2001.

[66] Masashi Sugiyama, Taiji Suzuki, and Takafumi Kanamori. *Density Ratio Estimation in Machine Learning*. Cambridge University Press, 2012.

[67] Shahzar Rizvi, Mariel Pettee, and Benjamin Nachman. Learning likelihood ratios with neural network classifiers. *Journal of High Energy Physics*, 2024(2), February 2024.

[68] Alexey Dosovitskiy, Lucas Beyer, Alexander Kolesnikov, Dirk Weissenborn, Xiaohua Zhai,

Thomas Unterthiner, Mostafa Dehghani, Matthias Minderer, Georg Heigold, Sylvain Gelly, et al. An image is worth 16x16 words: Transformers for image recognition at scale. *arXiv preprint arXiv:2010.11929*, 2020.

[69] Martín Abadi, Paul Barham, Jianmin Chen, Zhifeng Chen, Andy Davis, Jeffrey Dean, Matthieu Devin, Sanjay Ghemawat, Geoffrey Irving, Michael Isard, et al. Tensorflow: A system for large-scale machine learning. *OSDI*, 16:265, 2016.

[70] Fraciois Chollet. Keras. https://github.com/fchollet/keras, 2017.

[71] Xiangning Chen, Chen Liang, Da Huang, Esteban Real, Kaiyuan Wang, Hieu Pham, Xuanyi Dong, Thang Luong, Cho-Jui Hsieh, Yifeng Lu, et al. Symbolic discovery of optimization algorithms. *Advances in Neural Information Processing Systems*, 36, 2024.

[72] Roman Kogler. Measurement of jet production in deep-inelastic ep scattering at hera, Feb 2011.

[73] V. Andreev et al. Measurement of multijet production in ep collisions at high Q^2 and determination of the strong coupling α_s. *Eur. Phys. J. C*, 75(2):65, 2015.

[74] F. D. Aaron et al. Measurement of $D^{*\pm}$ Meson Production and Determination of $F_2^{c\bar{c}}$ at low Q^2 in Deep-Inelastic Scattering at HERA. *Eur. Phys. J. C*, 71:1769, 2011. [Erratum: Eur.Phys.J.C 72, 2252 (2012)].

[75] F. D. Aaron et al. Inclusive Deep Inelastic Scattering at High Q^2 with Longitudinally Polarised Lepton Beams at HERA. *JHEP*, 09:061, 2012.

[76] B. Efron. Bootstrap Methods: Another Look at the Jackknife. *The Annals of Statistics*, 7(1):1 – 26, 1979.

[77] V. Andreev, M. Arratia, Baghdasaryan, et al. Measurement of lepton-jet correlation in deep-inelastic scattering with the h1 detector using machine learning for unfolding. *Phys. Rev. Lett.*, 128:132002, Mar 2022.

[78] Xiaohui Liu, Felix Ringer, Werner Vogelsang, and Feng Yuan. Lepton-jet correlations in deep inelastic scattering at the Electron-Ion Collider. *Phys. Rev. Lett.*, 122(19):192003, 2019.